JACS
JOURNAL OF THE AMERICAN CHEMICAL SOCIETY
Article
pubs.acs.org/JACS

# Surface Plasmon Resonance Enhanced Light Absorption and Photothermal Therapy in the Second Near-Infrared Window

Xianguang Ding,[†,‡] Chi Hao Liow,[§] Mengxin Zhang,[‡] Renjun Huang,[∥] Chunyan Li,[†,‡] He Shen,[‡] Mengya Liu,[†,‡] Yu Zou,[†,‡] Nan Gao,[†,‡] Zhijun Zhang,[‡] Yonggang Li,[∥] Qiangbin Wang,[†,‡] Shuzhou Li,[§] and Jiang Jiang*[,†,‡]

[†]i-Lab, Suzhou Institute of Nano-Tech and Nano-Bionics, Chinese Academy of Sciences, Suzhou 215123, China

[‡]Key Laboratory of Nano-Bio Interface, Division of Nanobiomedicine, Suzhou Institute of Nano-Tech and Nano-Bionics, Chinese Academy of Sciences, Suzhou 215123, China

[§]School of Materials Science and Engineering, Nanyang Technological University, 50 Nanyang Avenue, Singapore 639798

[∥]Department of Radiology, The First Affiliated Hospital of Soochow University, Suzhou 215006, China

Supporting Information

**ABSTRACT:** Enhanced near-field at noble metal nanoparticle surfaces due to localized surface plasmon resonance (LSPR) has been researched in fields ranging from biomedical to photoelectrical applications. However, it is rarely explored on nonmetallic nanomaterials discovered in recent years, which can also support LSPR by doping-induced free charge carriers, let alone the investigation of an intricate system involving both. Here we construct a dual plasmonic hybrid nanosystem Au−$Cu_9S_5$ with well controlled interfaces to study the coupling effect of LSPR originating from the collective electron and hole oscillations. $Cu_9S_5$ LSPR is enhanced by 50% in the presence of Au, and the simulation results confirm the coupling effect and the enhanced local field as well as the optical power absorption on $Cu_9S_5$ surface. This enhanced optical absorption cross section, high photothermal transduction efficiency (37%), large light penetration depth at 1064 nm, excellent X-ray attenuation ability, and low cytotoxicity enable Au−$Cu_9S_5$ hybrids for robust photothermal therapy in the second near-infrared (NIR) window with low nanomaterial dose and laser flux, making them potential theranostic nanomaterials with X-ray CT imaging capability. This study will benefit future design and optimization of photoabsorbers and photothermal nanoheaters utilizing surface plasmon resonance enhancement phenomena for a broad range of applications.

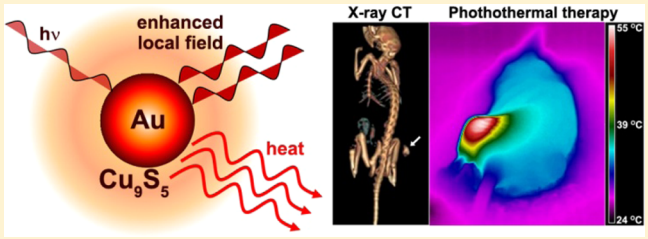


## INTRODUCTION

Localized surface plasmon resonance (LSPR) arises from the collective oscillation of free charge carriers in nanoparticles (NPs) driven by the electromagnetic field of incident light.[1] This strong light-matter interaction generates locally enhanced electromagnetic field, which has spurred great interest for its application in enhanced optical phenomena, photocatalysis, and optoelectronic control.[2−9] The most studied plasmonic NPs are noble metals of Au, Ag, and Cu, which support LSPR in the visible spectrum. However, the discovery of LSPR in semiconductor nanocrystals of nonstoichiometric copper chalcogenides has opened up a new regime in plasmonics.[10,11] $Cu_{2-x}E$ (E = S, Se, Te) NPs are p-doped due to copper deficiency, resulting large amount of hole carriers with high mobility, which support LSPR in the near-infrared (NIR). Since then, other heavily doped semiconductor nanomaterials and metal oxide nanocrystals have also been found to exhibit LSPR.[12−15] While LSPRs of noble metal nanostructures have been intensively studied for their ability to enhance local field, so far, few studies utilize LSPR sustained by heavily doped semiconductor as near-field nanoantennas.[16] Moreover, unlike a lot of work on noble metal NP dimers,[17−20] there is almost no report on plasmonic coupling between metal nanostructures and semiconductors.[21] In particular, whether the enhanced near-field at metal NPs surface could influence the collective hole oscillation in the neighboring heavily doped semiconductor, or vise versa, remains to be answered.[22]

Due to the dynamic tunability of LSPR by simple doping,[23,24] the heavily doped NPs have emerged as novel optical probes for redox reactions and photoelectrochemistry.[25,26] In addition, they have been extensively used as photothermal transducing agents in biomedical applications for their strong absorption in NIR.[27−31] Thermal therapy exploits local heating effect to kill cancer cells which are poorly vascularized,[32] and the employment of NIR light as a remote stimulus allows high spatial and temporal control of local heating while minimizing adverse side effects. To achieve effective tissue heating, two essential criteria, minimum tissue absorption and scattering to allow large light penetration depth while keeping tissue self-heating to a

Received: August 22, 2014
Published: October 23, 2014

   dx.doi.org/10.1021/ja508641z | J. Am. Chem. Soc. 2014, 136, 15684−15693

minimum, and high conversion of photon energy to heat by the photoabsorbers, have to be met. Great efforts have been devoted to develop new agents with high optical cross sections and photothermal transduction efficiency.[33−36] However, few have explored the role of excitation light. In particular, current research mainly focuses on the first NIR (NIR-I) window (700−950 nm), while the second NIR (NIR-II) window (1000−1350 nm) has been investigated less. Compared to the well studied NIR-I window, working in NIR-II window has two advantages: larger penetration depth and higher maximum permissible exposure (MPE) to laser. Penetration depth is expected to be maximal for 1000−1100 nm light,[37] and MPE for skin exposure is 1 W/cm$^2$ at this spectral region, compared to 0.33 W/cm$^2$ at 808 nm (ANSI Z136.1−2007, American National Standard for Safe Use of Lasers). While working in NIR-II window has attracted some attention in biological imaging,[38−41] up to now, it has rarely been used for photothermal therapy. The reason is ascribed to the lack of photosensitive materials of small sizes exhibiting strong absorption and high photothermal transduction efficiency in NIR-II window.[42,43] Very recently, Yeh et al. have reported synthesizing an Au rod-in-shell structure for photothermal therapy in NIR-II regime;[43] however, the power density (>2 W/cm$^2$) used was well above the safe limit for laser exposure, which may impede its future application.

To study the influence of surface-enhanced near-field at noble metal NPs surface on the collective hole oscillation in the neighboring NPs, and to construct photoabsorbers working in NIR-II window with high photothermal transduction efficiency, herein, we have designed a dual plasmonic Au−$Cu_9S_5$ nanostructure. The synthesized high purity Au−$Cu_9S_5$ hybrid NPs exhibit LSPRs in both visible and NIR region. The molar extinction coefficient of the hybrid NP is measured and compared to that of its individual components (Au and $Cu_9S_5$). A 50% enhanced absorption at 1064 nm as well as photothermal heating are observed, and theoretical calculation is performed to interpret this effect. The photothermal transduction efficiency and light penetration depth at 1064 nm are also determined. After establishing their photothermal ablation ability in vitro and low cytotoxicity, in vivo photothermal therapy on tumor-bearing mice using Au−$Cu_9S_5$ hybrids has been achieved with 100 ppm dose under 0.6 W/cm$^2$ 1064 nm laser irradiation. Furthermore, Au−$Cu_9S_5$ hybrids have been demonstrated as an attractive multifunctional platform for theranostic application combining X-ray computed tomography (CT) imaging and photothermal therapy capabilities all in one nanostructure system.

## EXPERIMENTAL SECTION

**Synthesis of Cu-Stearate.** 1.1 g of $CuCl_2$ and 4.75 g of sodium stearate were dissolved in methanol separately, which were then mixed and heated up to 70 °C for 3 h. After the solution was cooled down, the obtained product was washed with water and methanol three times and then dried for further use.

**Synthesis of Au NPs.** 10 nm diameter Au NPs were synthesized following the procedure reported by Mark T. Swihart and co-workers.[44] In brief, 5 mL of oleylamine (OAm) was heated up to 150 °C under $N_2$ atmosphere. After holding at this temperature for 20 min, 0.3 mmol $HAuCl_4$ in 1 mL of oleylamine was quickly injected into the hot OAm solution. The solution was allowed to stir for 90 min and then cooled to room temperature naturally. The particles were isolated by adding ethanol and washed with hexane.

**Synthesis of $Cu_9S_5$ NPs.** 188.1 mg of Cu-stearate was added into 5 mL of trioctylamine and stirred for 30 min under $N_2$ atmosphere to remove $O_2$. The solution was then heated up to 80 °C until a clear dark green solution was formed, at which point, 0.75 mL of sulfur solution prepared by dissolving 24 mg of elemental sulfur in 0.5 mL of 1,2-dichlorobenzene (DCB) and 2 mL of oleylamine was slowly added into the solution, followed by raising the solution temperature to 100 °C. The mixture was allowed to react at this temperature for 60 min, cooled down, and purified by several hexane and ethanol washing steps to isolate the $Cu_9S_5$ NPs.

**Synthesis of Au−$Cu_9S_5$ NPs.** 0.1 mmol Au NPs was mixed with 62.7 mg of Cu-stearate and added into 5 mL of trioctylamine. After 30 min stirring under $N_2$ to remove $O_2$, the solution temperature was raised to 80 °C, and 0.75 mL of sulfur solution prepared by dissolving 8 mg of elemental sulfur in 0.5 mL of DCB and 2 mL of oleylamine was then added dropwise. Immediately after the addition of S, solution color turned to dark purple, indicating the formation of hybrid NPs. The reaction mixture was heated up and maintained at 100 °C for 1 h, and then cooled to room temperature. The purification of the Au−$Cu_9S_5$ NPs was carried out by repeated washing and centrifuging with hexane and ethanol. The obtained NPs were redispersed in chloroform for further usage.

**Synthesis of Au Nanorods.** Gold nanorods with longitudinal surface plasmon resonance centered at ∼1070 nm were synthesized using a seed-mediated approach following the reported method.[45] Briefly, seed solution was first prepared by adding 1 mL of fresh 6 mM $NaBH_4$ solution into the 10 mL mixture consisting of 5 mL of 0.5 mM $HAuCl_4$ and 5 mL of 0.2 M CTAB, which then underwent vigorous stirring for 2 min and aged at 28 °C for 30 min. To prepare the growth solution, 7.0 g of CTAB and 1.234 g of sodium oleate were dissolved in 250 mL of hot water (∼50 °C). After being cooled to 28 °C, 24 mL of 4 mM $AgNO_3$ solution was added in, and the mixture was kept undisturbed at 30 °C for 15 min, until then 250 mL of 1 mM $HAuCl_4$ solution was added. After 90 min gentle stirring, 3.6 mL of 12 M HCl was introduced into this solution. Another 15 min later, 1.25 mL of 0.064 M ascorbic acid (AA) was added in, and the solution was vigorously stirred for 30 s. Finally, 0.8 mL of seed solution was injected into this growth solution and stirred for 30 s. The Au NR can be harvested after keeping the growth solution undisturbed at 28 °C for 8 h.

**Synthesis of $PMHC_{18}$−$PEG_{5000}$ Polymer.** 50 mg of poly(maleic anhydride-*alt*-1-octadecene) and 143 mg of PEG-$NH_2$ were dissolved together in 7.5 mL of DMSO/pyridine (7:1 volume ratio) mixture solution. After stirring for 12 h, 11 mg of EDC was added and the solution was continued to stir overnight at room temperature. The solution was dried under the flow of $N_2$, and the product was redissolved in water. The polymer solution was dialyzed against water over 48 h with an 8−12 kDa molecular weight cutoff membrane, and then lyophilized to yield the final $PMHC_{18}$−$PEG_{5000}$ polymer.

**NP Phase Transfer with $PMHC_{18}$−$PEG_{5000}$ Polymer.** The as prepared Au−$Cu_9S_5$ particles were first dispersed in 8 mL of chloroform, then 2 mL of chloroform solution containing 15 mg of $PMHC_{18}$−$PEG_{5000}$ polymer was added in. The mixture solution was allowed to stir for 1 h at room temperature. After that, excess polymer was removed by repeated centrifugation at 14 000 rpm for 15 min and washing with water. The redispersed solution further went through a 0.45 $\mu$m syringe filter to remove large NP aggregates formed during this surface modification process. The purified NP solution was finally lyophilized as solid powders, which can be stably stored at 4 °C.

**Measurement of Photothermal Transduction.** To evaluate the photothermal transduction of Au−$Cu_9S_5$ NPs, 0.6 mL of aqueous dispersion of Au−$Cu_9S_5$ NPs of different concentrations were put in a cuvette, and exposed to a 1064 nm laser at different power densities for 5 min. A thermocouple probe with an accuracy of 0.1 °C was inserted into the NP solutions perpendicular to the laser path to avoid direct light irradiation on the probe. The temperature was recorded every 20 s by a digital thermometer.

**In Vitro Cytotoxicity.** HeLa and F81 cells were selected as examples of cancer and normal cells to evaluate the cytotoxicity of Au−$Cu_9S_5$ NPs. Cells in the log phase of growth were seeded in 96-well plates at the density of $7 \times 10^3$ cells per well and incubated 24 h for cell attachment. Au−$Cu_9S_5$ NPs solution was then diluted


dx.doi.org/10.1021/ja508641z | J. Am. Chem. Soc. 2014, 136, 15684−15693

appropriately in fresh culture media and added to the wells (200 $\mu$L). After 24 h of continuous exposure to various concentrations of Au–$Cu_9S_5$ NPs, the culture media were changed back to fresh culture media to remove free NPs in the solution, and cell viability was investigated by standard WST assays.

**In Vitro Photothermal Ablation of Cancer Cells.** HeLa cells were used to evaluate the photothermal ablation efficiency of Au–$Cu_9S_5$ NPs. HeLa cells were first seeded in 96-well plates at a density of $7 \times 10^3$ cells per well for 24 h, and washed with PBS solution for three times. After then, different concentrations of Au–$Cu_9S_5$ NPs were added into the wells, and the cells were then exposed to a 1064 nm laser with an output power density of 0.7 or 1 W/cm$^2$ for 4 or 7 min. Cell viability after photothermal treatment was evaluated by WST assays. For live/dead cell staining using calcein AM (calcein acetoxymethyl ester) and PI (propidium iodide), HeLa cells were seeded in 48-well plates. After the same procedures outlined above, the cells were stained with both calcein AM and PI, and then confocal fluorescence images were acquired by confocal laser scanning microscope.

**In Vivo Photothermal Therapy.** The CT26 tumor-bearing mice (female, 6 weeks old) were intratumorally injected with 100 $\mu$L of Au–$Cu_9S_5$ NPs (100 ppm of Cu) when the tumor diameter reached ~5 mm. For the controls, only equal volume of PBS buffer solution was injected into the tumor. The tumor sites of both experimental and control groups were then irradiated by a 1064 nm laser at power density of 0.6 W/cm$^2$ for 5 min. During the irradiation process, local temperature profiles were captured real time by a thermal imaging camera. All animal procedures were in agreement with institutional animal use and care committee and carried out ethically and humanely.

**In Vitro and In Vivo CT Imaging.** Au–$Cu_9S_5$ NPs solutions of different concentrations ranging from 1 to 10 mg/mL were placed in 5 mL tubes. Images were obtained and data were analyzed by recording the Hounsfield units (HUs) for regions of interest. CT images were reconstructed with CT values calculated from raw data using 3D-Med software. For in vivo studies, the tumor-bearing mice were anesthetized by intraperitoneal injection of trichloroacetaldehyde hydrate (10%) at a dosage of 40 mg/kg body weight. Then, 100 $\mu$L of Au–$Cu_9S_5$ (5 mg/mL of Au) were intratumorally injected. CT images were acquired before and after the NP administration for CT analysis.

**Chracterizations.** Transmission electron microscopy (TEM) images were taken using a FEI Technai G2 S-Twin at an accelerating voltage of 200 kV. X-ray diffraction (XRD) analyses were performed using a Bruker D8 Advance X-ray diffractometer (with Cu Ka radiation at 0.15418 nm). UV–vis–NIR spectra were obtained with a PerkinElmer Lambda 750 spectrophotometer. X-ray photoelectron spectra (XPS) analyses were conducted on a PHI 5000 VersaProbe spectrometer (ULVAC-PHI) using Al K$\alpha$ radiation (1486.71 eV). Au and Cu concentrations were measured by an Inductively Coupled Plasma Optical Emission Spectrometer (PerkinElmer ICP-OES 2100 DV). WST assay was conducted using a Biotek Elx 800 Microplate Reader. Fluorescence imaging was carried out on a Nikon Laser scanning confocal microscope. CT data were acquired using GE Discovery CT750HD (GE Medical System, Milwaukee, WI). Infrared thermal imaging was performed with an IR thermal camera (FLIR, USA).

## RESULTS AND DISCUSSION

**Synthesis and Characterization of Au–$Cu_9S_5$ NPs.** Au–$Cu_9S_5$ hybrid NPs were synthesized by a seeded growth method. Under our optimized conditions (see Experimental section for details), a high yield of ~99% hybrid NPs was obtained (by counting over 300 NPs), i.e., only ~1% free $Cu_9S_5$ NPs were observed among the Au–$Cu_9S_5$ hybrid NPs. Elemental analysis by ICP shows the mass ratio of Au to Cu is 3.02, namely their atomic ratio in NP is ~1:1, consistent with the starting reactant molar ratio. Figure 1a shows a representative TEM image of Au–$Cu_9S_5$ hybrid NPs with an

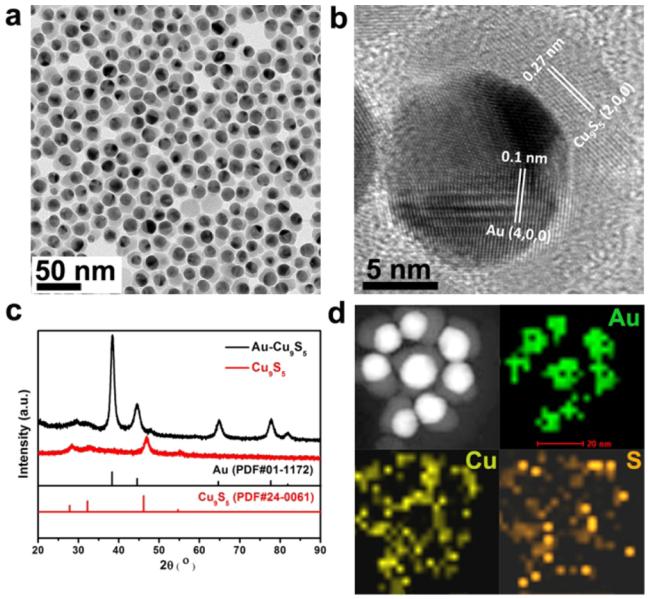


**Figure 1.** (a, b) TEM and HRTEM images of the synthesized Au–$Cu_9S_5$ NPs. (c) Powder X-ray diffraction patterns of Au–$Cu_9S_5$ and $Cu_9S_5$ NPs. (d) STEM image of Au–$Cu_9S_5$ NPs and their corresponding EDS elemental mapping images.

overall lateral dimension of ~20 nm, which clearly shows the high contrast 10 nm Au cores surrounded by the lighter $Cu_9S_5$ domains. In the corresponding high-resolution TEM (HRTEM) image (Figure 1b) of a single hybrid NP, the measured lattice spacing of 0.1 nm for the dark part and 0.27 nm for the light part correspond well to fcc Au (400) and hexagonal $Cu_9S_5$ (200) planes. The crystal structure of Au–$Cu_9S_5$ hybrid NPs was also examined by X-ray diffraction studies (Figure 1c). Two series of Bragg reflections were found, which can be assigned to fcc Au and hexagonal $Cu_9S_5$ respectively. However, poor crystallinity due to relatively low reaction temperature (100 °C) and heavy metal effect, make the identification of $Cu_9S_5$ phase in the hybrid nanostructures difficult. To further confirm the composition and illustrate the structure of the synthesized hybrids, elemental mapping by energy-dispersive X-ray spectroscopy (EDS) was performed on these hybrid nanocrystals. Figure 1d shows that the distributions of Cu and S element were largely colocalized, which however did not overlap with those of Au, indicating $Cu_9S_5$ was located around Au but did not encapsulate Au core fully.

For hybrid NPs formation, the molar ratio of starting Au and Cu was optimized to be 1:1. Below this ratio, many free $Cu_9S_5$ would form. The order of the addition of reactants was also critical, as when elemental sulfur was added first to Au NPs solution before Cu-precursor addition, the yield of hybrid can reach 100%; that is, no free $Cu_9S_5$ NPs were observed in the final product. However, this procedure also produced many Au NP aggregates surrounded by $Cu_9S_5$ domains (Supporting Information, Figure S1). It is postulated that the strong affinity between Au and sulfur induced Au NP aggregation due to surface ligand replacement and subsequent particle fusion.[46] The introduction of 1, 2-dichlorobenzene (DCB) solvent was also an indispensable factor for the formation of hybrid nanoparticles. Without DCB, only separate Au and $Cu_9S_5$ NPs were produced (Figure S2). The exact role of DCB in the hybrid formation is not clear yet. One possible explanation is


dx.doi.org/10.1021/ja508641z | J. Am. Chem. Soc. 2014, 136, 15684–15693

the increased solvent polarity might facilitate $Cu_9S_5$ nucleation around Au, which has been proposed for flower-like Au−$Fe_3O_4$ formation.[47]

**Optical Property of Au−$Cu_9S_5$ NPs.** The growth of plasmonic $Cu_9S_5$ NPs onto Au NPs gives Au−$Cu_9S_5$ hybrid NPs distinct optical properties. As shown in Figure 2a, two

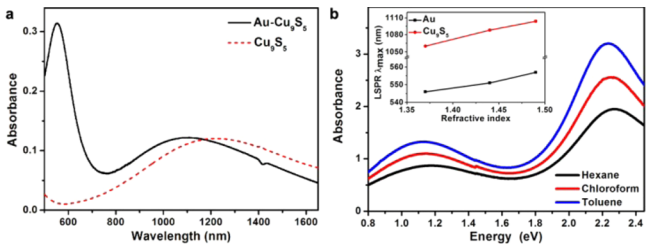


**Figure 2.** (a) UV−vis−NIR absorption spectra of colloidal solutions of the Au−$Cu_9S_5$ and $Cu_9S_5$ NPs dispersed in chloroform. (b) Absorption spectra of Au−$Cu_9S_5$ NPs in solvents with different refractive indexes, and the inset shows the plot of LSPR absorption peak wavelength with respect to increasing surrounding media refractive indexes.

intense absorption peaks in the visible and NIR region are present, arising separately from plasmon resonance of Au and $Cu_9S_5$ domains in the hybrid nanostructure. The peak centered at 550 nm in the visible region comes from the LSPR absorption of Au NPs. Compared with plain Au NP seeds showing a 520 nm absorption peak, the observed red-shift of plasmon resonance can be ascribed to the high refractive index of $Cu_9S_5$ (4.2) surrounding the core Au NPs. The absorption peak in the NIR centered at ∼1100 nm is assigned to the LSPR of $Cu_9S_5$ NPs, which is blue-shifted 125 nm compared to that of $Cu_9S_5$ NPs synthesized without Au seeds under the same experimental conditions. Due to the strong influence of particle size, structure, and surface ligand on $Cu_{2-x}S$ LSPR,[11,48,49] it is difficult to single out the determining factor for the observed blue-shift. The peak assignments to dual LSPR are corroborated by measuring the hybrid NPs absorption spectra in different solvents, as a key signature of LSPR is that its frequency depends sensitively on the dielectric constant of the surrounding medium. As shown in Figure 2b, when Au−$Cu_9S_5$ hybrid NPs were dispersed in three different solvents (hexane, chloroform, and toluene), both peaks in the visible and NIR region red-shifted as the refractive index of the surrounding media increased (Figure 2b inset), confirming the dual LSPR nature of the solution absorption. The LSPR sensitivity is calculated to be 367 nm per refractive index unit (nm/RIU) for $Cu_9S_5$ and 91 nm/RIU for Au.

For biomedical applications, these hydrophobic Au−$Cu_9S_5$ hybrid NPs have to be transferred into aqueous phase while maintaining their optical properties. This was achieved by amphiphilic poly(maleic anhydride-*alt*-1-octadecene)−$PEG_{5000}$ ($PMHC_{18}$−$PEG_{5000}$) polymer encapsulation, through hydrophobic−hydrophobic interaction between NP surface ligands and the amphiphilic polymer chains.[50] The absorption spectra before and after phase transfer process indicate the optical property was not affected by this phase transfer method, as shown in Figure S3. The presence of PEG ligands on the outer surfaces of Au−$Cu_9S_5$ NPs ensures their excellent dispersion in aqueous solutions, which can be kept stable up to several months (Figure S4)

**Photothermal Property of Au−$Cu_9S_5$ NPs.** Photothermal therapy is an emerging technique that makes use of photothermal agents converting photons into local heat, thus causing cancer cell death at the target tumor sites. As an efficient photoabsorber in the NIR region (especially 1000−1200 nm), Au−$Cu_9S_5$ NPs are expected to be good nanoheaters for cancer cell ablation. The photothermal effect of Au−$Cu_9S_5$ NPs was first studied by monitoring the temperature change of 0.6 mL of Au−$Cu_9S_5$ NPs solution under the irradiation of a 1064 nm cw laser. At laser power density of 0.7 W/cm$^2$, with the NP concentration varied from 6.25 to 50 ppm, the solution temperature elevation increased from 11.4 to 19.6 °C after 5 min laser irradiation, while pure water showed little heating at the same power density (Figure 3a). The above experimental parameters were selected so that a

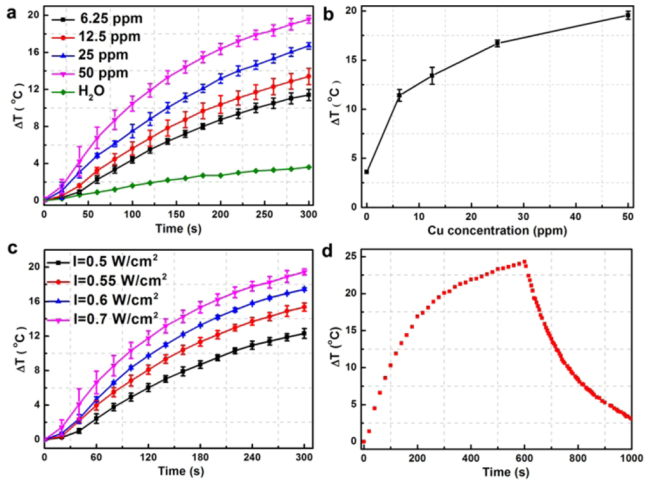


**Figure 3.** (a) Temperature elevation of plain water and Au−$Cu_9S_5$ NPs aqueous solutions at different concentrations under laser irradiation. (b) Plot of temperature change versus concentration of the $Cu_9S_5$ NPs after exposing to laser for 5 min, and 0 ppm stands for pure water. (c) Temperature elevation profiles of 50 ppm Au−$Cu_9S_5$ NPs aqueous solutions under different laser power densities. (d) The monitored temperature profile over 1000 s of a Au−$Cu_9S_5$ NPs aqueous solution (50 ppm) irradiated by laser for 600 s, followed by natural cooling with laser light turned off. Unless otherwise noted, a 1064 nm laser was used at a power density of 0.7 W/cm$^2$, and the error bars represent standard deviations ($n$ = 3).

proper solution temperature rise could be induced below MPE for 1064 nm laser. The final temperature rise at the end of the laser irradiation period as a function of NPs concentration is plotted in Figure 3b. From the figure, it is clear that the temperature elevation profile flattens out with increasing NP concentrations, due to the logarithmic absorbance dependence on the fraction of incident radiation.[51] When NPs concentration was fixed at 50 ppm, an obvious power density-dependent temperature rise was observed (Figure 3c). A temperature increase of 12.3 °C can be obtained with the incident laser power as low as 0.5 W/cm$^2$, which is well above the required temperature rise for efficient cancer photothermal therapy. In all of our solution photothermal measurements, the NP solutions were exposed to laser three times each, and no large variation of the temperature change was observed, indicating good photostability of the hybrid Au−$Cu_9S_5$ NPs.

The photothermal stability of Au−$Cu_9S_5$ NPs was further examined and benchmarked against Au nanorods by exposing the NPs under 1064 nm laser irradiation at the power density


dx.doi.org/10.1021/ja508641z | J. Am. Chem. Soc. 2014, 136, 15684−15693

of 1 W/cm$^2$, with their near-infrared absorption spectra and the corresponding TEM images taken before and after 30 min of laser illumination (Figures S5 and S6). The longitudinal LSPR absorption of Au nanorods blue-shifted and decreased in intensity (>20%) after laser exposure, indicating morphological changes to smaller aspect ratios due to melting and restructuring, which was also confirmed by TEM images, showing large spherical Au particle formation after being exposed to laser. While for Au−$Cu_9S_5$ hybrid NPs under the same conditions, there was no significant change (<5%) observed in the solution absorbance or nanostructure morphology, indicating their high photostability.

To quantify the photothermal transduction efficiency, calculation was performed based on the method first developed by Roper and co-workers (detailed in the Supporting Information).[51] NP dispersions were illuminated until reaching a steady state temperature, at which point the light source was removed, and the solution was allowed to cool down naturally. During this cooling stage, the temperature decrease was monitored to determine the rate of heat dissipation from the system to the environment (Figure 3d), which was obtained by fitting the measured cooling curve (Figure S7). By balancing the photon energy input and system heat dissipation at steady state, the photothermal transduction efficiency of Au−$Cu_9S_5$ NPs was calculated to be 37%, which is higher than the reported value for $Cu_9S_5$ NPs (~25%).[29] The improved transduction efficiency likely originates from the reduced NPs dimension, which scatter less compared to the larger ones.[52] These results clearly demonstrate that Au−$Cu_9S_5$ hybrid NPs are highly efficient and photostable photothermal agents.

**Enhanced Optical Absorption of Au−$Cu_9S_5$ NPs.** Other than the photothermal transduction efficiency, how strong the nanomaterials can convert photon energy also depends on the strength of light-matter interactions. NPs that support plasmon resonances often exhibit large extinction cross sections exceeding their geometric ones, which makes them ideal nanoheaters. To determine how effective these Au−$Cu_9S_5$ NPs absorb light, their molar extinction coefficient was measured. Optical absorbance of Au, $Cu_9S_5$, and Au−$Cu_9S_5$ NP solutions of various concentrations were first measured, with their corresponding elemental concentrations determined by inductively coupled plasma optical emission spectroscopy, and subsequently the NP concentrations calculated based on the average NP sizes estimated from their TEM images. Au NP size of 10 nm in diameter was used for the calculation; for $Cu_9S_5$ NPs synthesized under the same conditions, nanoplates with dimension of 14 × 14 × 4.5 nm were used based on their TEM image (Figure S8). The molar extinction coefficients of specific NPs were then obtained by linear regression of the solution absorbance at different concentrations according to the Beer−Lambert law. The calculated extinction cross sections were on the order of $10^8$ $M^{-1}$ $cm^{-1}$, in accordance with literature reported values for small Au and $Cu_{2-x}Se$ NPs.[28] Compared to Au seeds and $Cu_9S_5$ NPs synthesized under the same experimental conditions, Au−$Cu_9S_5$ hybrid NP solution showed a remarkably large increase in the optical absorption across a broad spectral range (Figure 4a). In particular, for the interest of photothermal therapy in the second NIR window, Au−$Cu_9S_5$ hybrid NPs exhibit a ~50% increment in extinction coefficient at 1064 nm, versus the simple sum of their individual components, that is, Au and $Cu_9S_5$ NPs. However, due to the size variation and shape irregularities of the NPs, the size and shape approximations adopted can add uncertainties to the calculated values plotted in Figure 4a.[53]

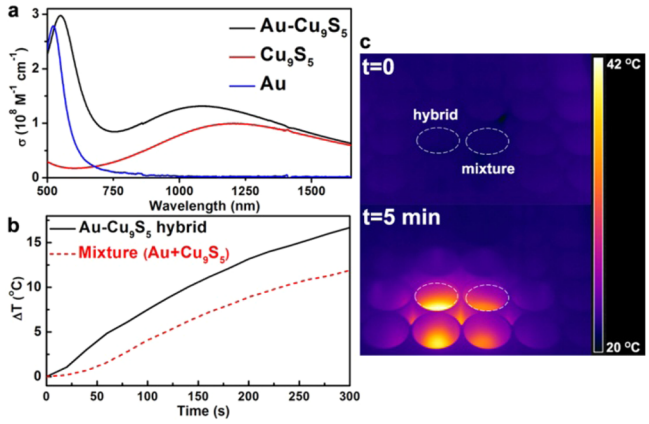


**Figure 4.** (a) Molar extinction coefficient ($\sigma$) of the Au−$Cu_9S_5$ nanoparticles and their corresponding components Au and $Cu_9S_5$ nanoparticles. (b) Temperature elevation profile of Au−$Cu_9S_5$ and the physical mixture of Au and $Cu_9S_5$ NPs at the same concentrations ($I$ = 0.7 W/cm$^2$, $t$ = 5 min). (c) Side-by-side comparison of temperature changes captured as thermal images upon light irradiation.

To better understand how this enhanced optical absorption contributes to the NPs photothermal conversion ability, the photothermal transduction of Au−$Cu_9S_5$ NPs was compared to the sum of their individual building blocks. When exposed to laser, the Au−$Cu_9S_5$ solution temperature increased by 17 °C, while only 12 °C increment was observed under exact irradiation conditions ($I$ = 0.7 W/cm$^2$, $t$ = 5 min) for the physical mixture of Au and $Cu_9S_5$ NPs at the same concentrations (Figure 4b). This effect can be better visualized by taking corresponding infrared thermographs for side-by-side comparison (Figure 4c). The results demonstrated here indicate that Au−$Cu_9S_5$ nanostructures are much more efficient nanoheaters than the simple physical mixture of their individual components, so that they could provide equivalent heating at reduced dosage, alleviating potential side effects and complications in clinical applications.

The photothermal energy input transduced by nanoparticles can be expressed as $Q_{NC} = I(1 - 10^{A\lambda})\eta$, where both solution absorbance ($A$) and photothermal transduction efficiency ($\eta$) contribute to the energy input that gives rise to solution temperature increase.[51] To investigate whether the enhanced heating was a result of absorption enhancement or by change of photothermal conversion efficiency upon Au−$Cu_9S_5$ nanocomposite formation, experiments were conducted with fixed nanomaterial dispersion absorbance ($A$) and laser intensity ($I$). Then, the solution temperature increment was solely determined by $\eta$. The Au−$Cu_9S_5$ and $Cu_9S_5$ NPs dispersions, which have the same absorbance at the laser illumination wavelength, were prepared and exposed to 1064 nm laser for 5 min. The measured temperature elevation curves of these two solutions showed nearly no difference as shown in Figure S9, indicating $\eta$ is an intrinsic property determined solely by the nature of the nanomaterials. Thus, it can be concluded that the photothermal transduction with NIR light irradiation is due to the plasmonic resonance absorption of $Cu_9S_5$ NPs, and the presence of Au in the hybrid nanostructures does not change their photothermal conversion efficiency. However, Au enhances $Cu_9S_5$ NP absorption in Au−$Cu_9S_5$ hybrids, thus effectively increases the molar extinction coefficient of Au−


dx.doi.org/10.1021/ja508641z | J. Am. Chem. Soc. 2014, 136, 15684−15693

$Cu_9S_5$ NPs in the NIR region, rendering them as more efficient nanoheaters.

**In Vitro Photothermal Cell Ablation.** Motivated by the excellent photothermal property of Au−$Cu_9S_5$ NPs in solution, we continued to examine the efficacy of Au−$Cu_9S_5$ NPs for cancer photothermal therapy in vitro in NIR-II window. Prior to using Au−$Cu_9S_5$ NPs for biomedical applications, their biocompatibility was first evaluated on F81 and HeLa cells, selected as a model system for normal and cancer cells, respectively. Figure 5a displays the cell viability after incubating

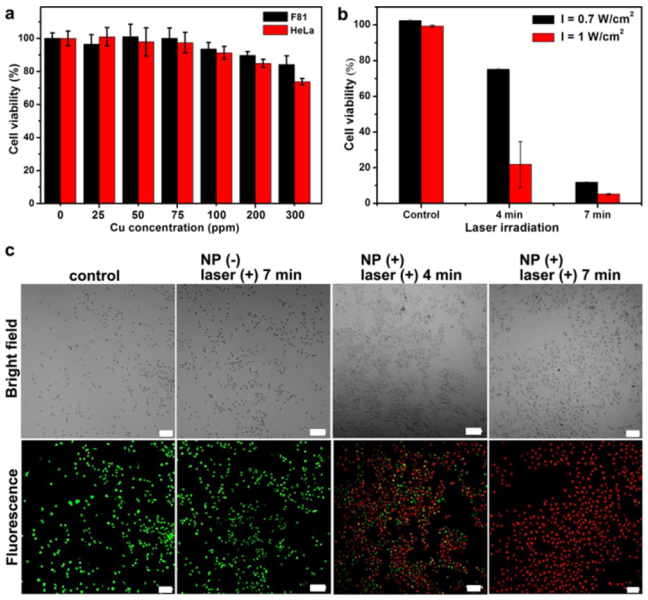


**Figure 5.** (a) Viabilities of the F81 and HeLa cells determined by WST assay after incubating the cells with various concentrations of Au−$Cu_9S_5$ NPs for 24 h. (b) Viabilities of HeLa cells after Au−$Cu_9S_5$ NPs (50 ppm) induced photothermal therapy under 1064 nm laser at different laser power densities and durations. (c) Bright field and fluorescence images of calcein AM and PI costained HeLa cells incubated without and with 50 ppm Au−$Cu_9S_5$ NPs, under 1064 nm light irradiation at a power density of 0.7 W/cm$^2$ for 4 or 7 min (scale bars represent 100 $\mu$m).

them with different concentrations of Au−$Cu_9S_5$ NPs for 24 h using standard WST assays. No obvious cytotoxicity was observed for both cell lines with NP concentration up to 300 ppm, and a recent study also showed CuS is biodegradable without significant toxicity.[54] Their photothermal cytotoxicity was evaluated by exposing HeLa cells to 1064 nm laser illumination. In the absence of Au−$Cu_9S_5$ NPs, HeLa cells stayed viable after being irradiated at power density up to 1 W/cm$^2$ for 7 min. However, with the addition of 50 $\mu$g/mL of Au−$Cu_9S_5$ NPs, cell viability decreased rapidly after laser illumination, with ∼10% of cells remained alive at a power density of 0.7 W/cm$^2$ for 7 min (Figure 5b). Moreover, phototoxicity depended on both laser power density and exposure duration.

Fluorescent live/dead cell staining experiments were performed to better visualize this photothermal ablation process. HeLa cells were stained with both calcein AM (green fluorescence) and propidium iodide (PI, red fluorescence) to show their viability under a laser confocal microscope. When the cells were incubated with NPs and exposed to laser, the number of live cells (green) decreased and dead cells (red) increased with longer laser irradiation time. When the irradiation duration reached 7 min, almost no green color can be observed, indicating cancer cells had all been effectively killed (Figure 5c), in agreement with the WST assay results presented in Figure 5b. In contrast, laser light alone did not cause any appreciable cell death. The above results clearly demonstrated that Au−$Cu_9S_5$ NPs can induce photothermal ablation of cancer cells in NIR-II window quickly (4−7 min) with low doses of NPs (50 ppm) under safe laser illumination intensity (1064 nm, 0.7 W/cm$^2$).

**Deep Tissue Photothermal Therapy in NIR-II Window.** The NIR-II window can offer larger tissue penetration depth relative to the commonly researched NIR-I window, due to lower absorption and scattering by tissues in this spectral range. We explored the deep tissue photothermal ability in NIR-II window using the synthesized Au−$Cu_9S_5$ NPs under 1064 nm laser irradiation, where pig epithelial tissues of varying thickness (2, 5, 7, 10, 15, and 20 mm) were prepared and used as model biological tissues. 24-well plates filled with 1.2 mL of Au−$Cu_9S_5$ NPs dispersion and covered by tissues of different thickness on top were subjected to 1064 nm laser irradiation (1 W/cm$^2$) for 7 min, and the infrared thermographs were then captured by a thermal imaging camera (Figure S10). Efficient heating of the solution was achieved without introducing significant heating inside the tissue. The measured temperature changes under different depth of tissues were normalized to the maximum temperature increase without tissue cover, plotted as a function of tissue depth, and fitted by an exponential decay curve. From the fitting curve, a decay length of 5.3 mm was obtained (Figure 6). This is in accordance to the value calculated by Bashkatov et al.,[37] showing the great promise of using Au−$Cu_9S_5$ NPs for deep tissue photothermal therapy in NIR-II window.

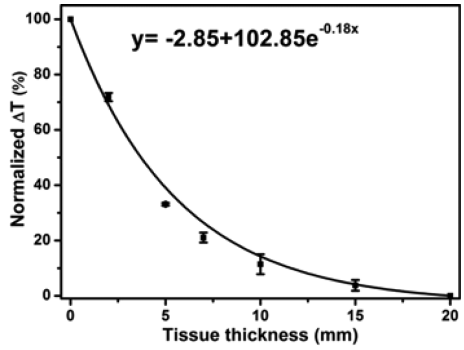


**Figure 6.** Scattered plot of the normalized temperature change under different tissue depth, with the fitted exponential decay curve. The error bars represent standard deviations ($n$ = 3).

**In Vivo Photothermal Therapy in NIR-II Window.** Encouraged by the in vitro photothermal results and the deep tissue penetration ability of light in NIR-II window, Au−$Cu_9S_5$ NPs for photothermal cancer cells ablation was further assessed in vivo. Nude mice bearing CT26 tumor model were injected intratumorally with 100 $\mu$L of aqueous dispersion of 100 $\mu$g/mL of Au−$Cu_9S_5$ hybrid NPs or blank PBS, and the tumors were then exposed to 1064 nm laser at a power density of 0.6 W/cm$^2$ for 5 min. The spatial temperature distribution at the tumor surface was monitored real-time by a thermal imaging camera. Since the highest temperature was generated at the photothermal agent injection site of 3−5 mm beneath skin, but not the tissue surface which was nearest to the laser (Figure S10), we speculate the temperature inside tumor was even


dx.doi.org/10.1021/ja508641z | J. Am. Chem. Soc. 2014, 136, 15684−15693

higher than the measured tumor surface temperature. As shown in Figure 7a,c, the temperature of the tumor regions with Au–$Cu_9S_5$ NPs increased rapidly from 35 to 54 °C in 2 min. In contrast, tumor injected with PBS only showed ~5 °C temperature change after the same laser irradiation treatment. The effect of NIR laser treatment on tumor with or without Au–$Cu_9S_5$ was evaluated by histology studies. Hematoxylin and eosin (H&E) staining demonstrated that Au–$Cu_9S_5$ NPs + NIR treated tumor tissues showed obvious necrosis, such as severe degree of cell shrinkage to lost contact, nuclear condensation, and the corruption of the tumor extracellular matrix. On the other hand, tumor tissues from PBS + NIR treatment showed no difference compared to normal healthy tissues (Figure 7d).

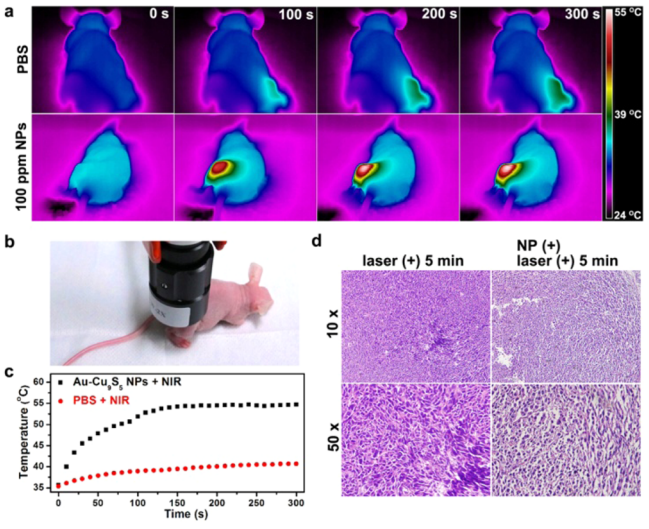


**Figure 7.** (a) Representative thermal images of tumor-bearing mice exposed to 1064 nm laser (0.6 W/cm$^2$, 5 min) after intratumorally injected with 100 $\mu$L of PBS (control) and Au–$Cu_9S_5$ NPs (100 $\mu$g/mL). (b) A photograph illustrating the experimental setup for in vivo photothermal treatment. (c) The corresponding temperature rise profiles at the tumor site over 5 min laser irradiation with NPs or PBS only. (d) H&E staining of tumor tissue sections at different magnifications after photothermal treatments with and without Au–$Cu_9S_5$ NPs.

**Au–$Cu_9S_5$ NPs as X-ray CT Contrast Enhancer.** Besides acting as a highly efficient photothermal transduction agent for cancer photothermal therapy, Au–$Cu_9S_5$ NPs were also investigated for contrast enhancement in CT imaging, which is a widely used medical imaging technique for diagnosis due to its deep tissue penetration and high resolution characteristics. High atomic number element such as Au has shown excellent X-ray attenuation ability, which triggered research on using biocompatible Au NPs as contrast enhancing agent for CT imaging.[55,56] The feasibility of the synthesized hybrid NPs to be a CT contrast enhancing agent was first examined in phantom (Figure 8a,b). The imaging contrast and HU values showed a well-correlated linear increment with increasing particle concentrations. Furthermore, in vivo CT contrast enhancing effect of the NPs was also evaluated on nude tumor-bearing mice with a clinical scanner. After being anesthetized, mice were intratumorally injected with 100 $\mu$L of Au–$Cu_9S_5$ NPs at a dosage of 0.5 mg (Au element), and CT images were acquired before and after injection (Figure 8c,d). High image contrast at the tumor sites could be observed after NP injection, as the tumor CT image became much brighter with the HU value increased from 43 to 470. The reconstructed three-dimensional (3D) CT image of the mouse clearly displayed enhanced contrast in the tumor region after intratumorally administered NPs, revealing that Au–$Cu_9S_5$ NPs can be simultaneously used as a contrast enhancing agent for tumor imaging.

**Au LSPR Enhances $Cu_9S_5$ Plasmonic Absorption.** LSPR at the noble metal NP surface can generate a strong local optical field that extends into the surrounding medium over 10 nm,[57] which gives rise to the phenomena such as surface-enhanced Raman scattering,[2] surface-enhanced luminescence,[5,6] and so forth. Moreover, this field enhancement can exist far from the resonant plasmon excitation energy.[58] To explore the possible contribution of local field enhancement to the observed enhanced absorption and photothermal properties of Au–$Cu_9S_5$ NPs, theoretical simulation using discrete dipole approximation (DDA) was performed.[59] The nanostructure used in DDA simulation is illustrated schematically in Figure 9a, denoted as UFO-like nanostructure, where the Au nanosphere sits in the middle of a $Cu_9S_5$ nanoring. This structure is proposed on the basis of the observed hybrid NP morphology and its elemental mapping result as shown in Figure 1. Then, the electric field enhancements of each individual nanoparticles and their assembled UFO nanostructure were calculated, with the electric field distribution at several set wavelengths plotted in Figure 9b. The overall

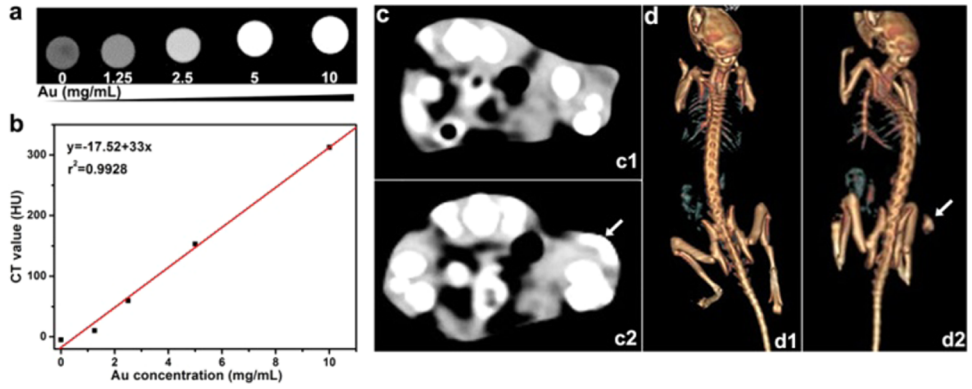


**Figure 8.** (a) CT images and (b) CT value (HU) of Au–$Cu_9S_5$ NPs dispersion as a function of the particle concentrations. Cross-sectional CT images of tumor before (c1) and after injection of Au–$Cu_9S_5$ NPs (c2), and their corresponding 3D reconstructed CT images before (d1) and after injection (d2) of Au–$Cu_9S_5$ NPs. The arrow heads point to the tumor sites.


dx.doi.org/10.1021/ja508641z | J. Am. Chem. Soc. 2014, 136, 15684–15693

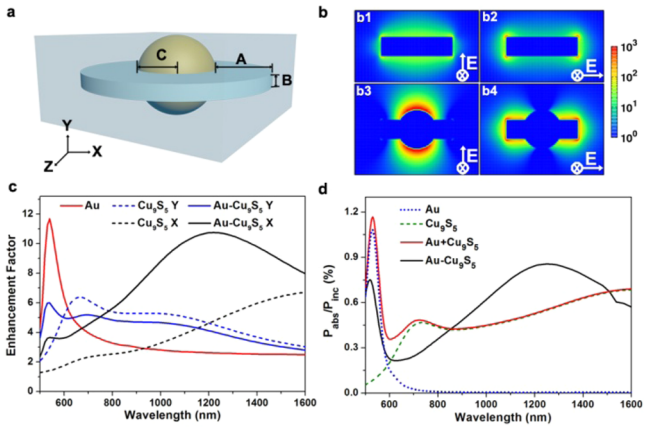


**Figure 9.** (a) Schematic drawing of Au−$Cu_9S_5$ UFO-like nanostructure with dimensions of $A$ = 5 nm, $B$ = 6 nm, and $C$ = 6 nm. (b) Electric field distribution of $Cu_9S_5$ at 660 nm (b1, Y polarization) and 1600 nm (b2, X polarization), Au−$Cu_9S_5$ at 540 nm (b3, Y polarization) and 1220 nm (b4, X polarization). (c) DDA calculated average electric field enhancement corresponding to Au, $Cu_9S_5$ in Y and X polarization directions, and Au−$Cu_9S_5$ hybrid in Y and X polarization directions. (d) DDA calculated integrated optical power absorption of Au, $Cu_9S_5$, sum of Au and $Cu_9S_5$, and Au−$Cu_9S_5$ hybrid as a function of wavelength.

average electric field enhancement profile red-shifts compared to the far field spectra, which is a universal law when comparing far field to near field of the same structures.[60] $Cu_9S_5$ nanodisks excited along X or Y polarizations show only half the enhancement factor of Au nanospheres (Figure 9b and Figure S11). As for UFO nanostructures, Y polarization has shown an enhanced peak around 540 nm (Figure 9c), which is attributed to the Au surface plasmon resonance, where one can see a strong electric field tightly confined around the Au surface and little around $Cu_9S_5$ nanoring (Figure 9b3). On the other hand, with X polarized excitation, strong field enhancement comparable to single Au nanosphere is obtained in NIR. Taking note of the peak around 660 nm in simulation result, arising from transverse SPR mode of $Cu_9S_5$ nanoplate,[61] is absent in measured solution absorption spectra, and similar observation has also been reported.[62] Power absorbed can be then calculated on the basis of the simple equation $P_{abs} = 1/2\omega\varepsilon''|E|^2$, where $\omega$ represents the frequency, $\varepsilon''$ represents the imaginary part of the dielectric permittivity, and $E$ is the total electric field.[63,64] The power absorption spectra for isolated $Cu_9S_5$, Au, their mixture as well as hybrids are illustrated in Figure 9d. The blue-shift of the simulated longitudinal SPR mode in the hybrid NPs qualitatively agrees with experimental results. At 1064 nm, calculated results show a 51% increase in absorption in the hybrids, in agreement with experimental observations. By integrating area under the curves, hybrid UFO structure absorbs ∼25% more than $Cu_9S_5$ in the spectral region from 500 to 1600 nm. Our calculation shows although the NIR-II region is far from Au surface plasmon resonance (∼550 nm), Au still exhibits local field enhancement, and this enhanced near-field and SPR coupling account for the observed enhanced NIR absorption in Au−$Cu_9S_5$ hybrids. However, the power absorbed can vary due to the size and shape irregularity,[53] and possible structural effect. Therefore, simulation model and results obtained based on approximations made from TEM micrographs only qualitatively represents the similar trend as experimental observations. Furthermore, work on optimizing hybrid NP synthesis to maximize the local field enhancement, including tuning Au nanostructure plasmon resonances closer to NIR window, are still needed in order to gain even more efficient nanoheaters.

The mutual interaction of each domain in a complex system such as Au−$Cu_9S_5$ hybrids, which include both free electron-based LSPR in the Au domain and free hole-based LSPR in the $Cu_9S_5$ domain, can go far beyond the simple field enhancement effect as described above. For instance, Swihart and co-workers used a quantum junction model to analyze the interplay between Au and $Cu_{2-x}Se$ domain of the Au−$Cu_{2-x}Se$ heterodimer NPs, and proposed that holes could diffuse into the Au domain from the $Cu_{2-x}Se$ side, which led to decreased carrier concentration in $Cu_{2-x}Se$, and subsequent depressed and broadened NIR LSPR.[65] In another report, a contradictory conclusion is made, as interfacial electron transfer from the excited $Cu_2S$ to Au was proposed.[66] For Au−$Cu_9S_5$ hybrids reported here, XPS result indicated possible electron transfer from $Cu_9S_5$ to Au (Figure S12), which could lead to increased carrier concentration in $Cu_9S_5$ and enhanced blue-shifted LSPR. Substantial work remains to be done in order to elucidate the existence and role of electron transfer to the plasmonic coupling between metal and semiconductor NPs.

## CONCLUSION

A dual plasmonic hybrid system Au−$Cu_9S_5$ NPs is developed to investigate the coupling of the collective hole oscillation in the heavily doped semiconductors with the surface-enhanced near-field at noble metal NPs surfaces. The Au−$Cu_9S_5$ hybrid NPs exhibit a 50% increase in absorbance at 1064 nm compared to $Cu_9S_5$ NPs synthesized under the same conditions. This enhanced absorption translates to improved heating of the hybrids compared to the simple mixture of Au and $Cu_9S_5$ with the same dose of Au and Cu. DDA calculation has shown the redistributed and enhanced local field at Au−$Cu_9S_5$ surface, indicating strong interaction between Au and $Cu_9S_5$ domains in the hybrid. Moreover, Au−$Cu_9S_5$ NPs show excellent colloidal and photo stability. Their large absorption cross section ($1.3 \times 10^8$ $M^{-1}$ $cm^{-1}$), high photothermal transduction efficiency (37%), large tissue penetration depth of over 5 mm at 1064 nm, and low cytotoxicity enable Au−$Cu_9S_5$ hybrids for excellent in vitro and in vivo cancer cells photothermal ablation in NIR-II window. To the best of our knowledge, this is the first report on photothermal therapy in NIR-II windows with power density lower than laser safety standards. In addition, the Au−$Cu_9S_5$ NPs provide excellent CT imaging potential, which makes them potential candidate for future theranostic applications. Optimizing the Au−$Cu_9S_5$ hybrids enrichment inside the tumor mass through active targeting and intravenous injection, studying their plasma half-life, biodistribution, as well as in vivo cytotoxicity still need further investigations.

## ASSOCIATED CONTENT

### Supporting Information

Detailed photothermal transduction efficiency calculation and DDA simulations; additional TEM images and data. This material is available free of charge via the Internet at http://pubs.acs.org.

## AUTHOR INFORMATION

### Corresponding Author

jjiang2010@sinano.ac.cn

### Notes

The authors declare no competing financial interest.

## ■ ACKNOWLEDGMENTS

This work was funded by the "Hundred Talents" program of the Chinese Academy of Sciences, the Natural Science Foundation of China (Grant No. 21473243 and 51202283), and Singapore MOE Tier 2 (ACR 12/12). We thank Prof. Xuefeng Gao for the use of IR thermal camera.

## ■ REFERENCES

(1) Eustis, S.; El-Sayed, M. A. *Chem. Soc. Rev.* **2006**, *35*, 209.
(2) Nie, S. M.; Emery, S. R. *Science* **1997**, *275*, 1102.
(3) Atwater, H. A.; Polman, A. *Nat. Mater.* **2010**, *9*, 205.
(4) Schuller, J. A.; Barnard, E. S.; Cai, W. S.; Jun, Y. C.; White, J. S.; Brongersma, M. L. *Nat. Mater.* **2010**, *9*, 193.
(5) Punj, D.; Mivelle, M.; Moparthi, S. B.; van Zanten, T. S.; Rigneault, H.; van Hulst, N. F.; Garcia-Parajo, M. F.; Wenger, J. *Nat. Nanotechnol.* **2013**, *8*, 512.
(6) Gandra, N.; Portz, C.; Tian, L.; Tang, R.; Xu, B.; Achilefu, S.; Singamaneni, S. *Angew. Chem., Int. Ed.* **2014**, *53*, 866.
(7) Li, J. T.; Cushing, S. K.; Zheng, P.; Meng, F. K.; Chu, D.; Wu, N. Q. *Nat. Commun.* **2013**, *4*, 8.
(8) Scaiano, J. C.; Stamplecoskie, K. *J. Phys. Chem. Lett.* **2013**, *4*, 1177.
(9) Clavero, C. *Nat. Photonics* **2014**, *8*, 95.
(10) Zhao, Y.; Pan, H.; Lou, Y.; Qiu, X.; Zhu, J.; Burda, C. *J. Am. Chem. Soc.* **2009**, *131*, 4253.
(11) Luther, J. M.; Jain, P. K.; Ewers, T.; Alivisatos, A. P. *Nat. Mater.* **2011**, *10*, 361.
(12) Huang, Q.; Hu, S.; Zhuang, J.; Wang, X. *Chem.—Eur. J.* **2012**, *18*, 15283.
(13) Manthiram, K.; Alivisatos, A. P. *J. Am. Chem. Soc.* **2012**, *134*, 3995.
(14) Comin, A.; Manna, L. *Chem. Soc. Rev.* **2014**, *43*, 3957.
(15) Liu, X.; Swihart, M. T. *Chem. Soc. Rev.* **2014**, *43*, 3908.
(16) Li, W.; Zamani, R.; Rivera Gil, P.; Pelaz, B.; Ibáñez, M.; Cadavid, D.; Shavel, A.; Alvarez-Puebla, R. A.; Parak, W. J.; Arbiol, J.; Cabot, A. *J. Am. Chem. Soc.* **2013**, *135*, 7098.
(17) Encina, E. R.; Coronado, E. A. *J. Phys. Chem. C* **2011**, *115*, 15908.
(18) Sun, Y.; Foley, J. J.; Peng, S.; Li, Z.; Gray, S. K. *Nano Lett.* **2013**, *13*, 3958.
(19) Brown, L. V.; Sobhani, H.; Lassiter, J. B.; Nordlander, P.; Halas, N. J. *ACS Nano* **2010**, *4*, 819.
(20) Halas, N. J.; Lal, S.; Chang, W.-S.; Link, S.; Nordlander, P. *Chem. Rev.* **2011**, *111*, 3913.
(21) Lakshmanan, S. B.; Zou, X. J.; Hossu, M.; Ma, L.; Yang, C.; Chen, W. *J. Biomed. Nanotechnol.* **2012**, *8*, 883.
(22) Jiang, R.; Li, B.; Fang, C.; Wang, J. *Adv. Mater.* **2014**, *26*, 5274.
(23) Dorfs, D.; Härtling, T.; Miszta, K.; Bigall, N. C.; Kim, M. R.; Genovese, A.; Falqui, A.; Povia, M.; Manna, L. *J. Am. Chem. Soc.* **2011**, *133*, 11175.
(24) Kriegel, I.; Jiang, C.; Rodríguez-Fernández, J.; Schaller, R. D.; Talapin, D. V.; da Como, E.; Feldmann, J. *J. Am. Chem. Soc.* **2011**, *134*, 1583.
(25) Jain, P. K.; Manthiram, K.; Engel, J. H.; White, S. L.; Faucheaux, J. A.; Alivisatos, A. P. *Angew. Chem., Int. Ed.* **2013**, *52*, 13671.
(26) Cheng, H.; Kamegawa, T.; Mori, K.; Yamashita, H. *Angew. Chem., Int. Ed.* **2014**, *53*, 2910.
(27) Li, Y. B.; Lu, W.; Huang, Q. A.; Huang, M. A.; Li, C.; Chen, W. *Nanomedicine* **2010**, *5*, 1161.
(28) Hessel, C. M.; P. Pattani, V.; Rasch, M.; Panthani, M. G.; Koo, B.; Tunnell, J. W.; Korgel, B. A. *Nano Lett.* **2011**, *11*, 2560.
(29) Tian, Q. W.; Jiang, F. R.; Zou, R. J.; Liu, Q.; Chen, Z. G.; Zhu, M. F.; Yang, S. P.; Wang, J. L.; Wang, J. H.; Hu, J. Q. *ACS Nano* **2011**, *5*, 9761.
(30) Chen, Z.; Wang, Q.; Wang, H.; Zhang, L.; Song, G.; Song, L.; Hu, J.; Wang, H.; Liu, J.; Zhu, M.; Zhao, D. *Adv. Mater.* **2013**, *25*, 2095.
(31) Tian, Q. W.; Hu, J. Q.; Zhu, Y. H.; Zou, R. J.; Chen, Z. G.; Yang, S. P.; Li, R. W.; Su, Q. Q.; Han, Y.; Liu, X. G. *J. Am. Chem. Soc.* **2013**, *135*, 8571.
(32) Habash, R. W. Y.; Bansal, R.; Krewski, D.; Alhafid, H. T. *Crit. Rev. Biomed. Eng.* **2006**, *34*, 459.
(33) Zedan, A. F.; Moussa, S.; Terner, J.; Atkinson, G.; El-Shall, M. S. *ACS Nano* **2012**, *7*, 627.
(34) Lim, D.-K.; Barhoumi, A.; Wylie, R. G.; Reznor, G.; Langer, R. S.; Kohane, D. S. *Nano Lett.* **2013**, *13*, 4075.
(35) Lin, M.; Guo, C.; Li, J.; Zhou, D.; Liu, K.; Zhang, X.; Xu, T.; Zhang, H.; Wang, L.; Yang, B. *ACS Appl. Mater. Interfaces* **2014**, *6*, 5860.
(36) Li, B.; Wang, Q.; Zou, R.; Liu, X.; Xu, K.; Li, W.; Hu, J. *Nanoscale* **2014**, *6*, 3274.
(37) Bashkatov, A. N.; Genina, E. A.; Kochubey, V. I.; Tuchin, V. V. *J. Phys. D: Appl. Phys.* **2005**, *38*, 2543.
(38) Smith, A. M.; Mancini, M. C.; Nie, S. M. *Nat. Nanotechnol.* **2009**, *4*, 710.
(39) Welsher, K.; Liu, Z.; Sherlock, S. P.; Robinson, J. T.; Chen, Z.; Daranciang, D.; Dai, H. J. *Nat. Nanotechnol.* **2009**, *4*, 773.
(40) Hong, G.; Robinson, J. T.; Zhang, Y.; Diao, S.; Antaris, A. L.; Wang, Q.; Dai, H. *Angew. Chem., Int. Ed.* **2012**, *51*, 9818.
(41) Rocha, U.; Kumar, K. U.; Jacinto, C.; Villa, I.; Sanz-Rodríguez, F.; del Carmen Iglesias de la Cruz, M.; Juarranz, A.; Carrasco, E.; van Veggel, F. C. J. M.; Bovero, E.; Solé, J. G.; Jaque, D. *Small* **2014**, *10*, 1141.
(42) Maestro, L. M.; Haro-Gonzalez, P.; del Rosal, B.; Ramiro, J.; Caamano, A. J.; Carrasco, E.; Juarranz, A.; Sanz-Rodriguez, F.; Sole, J. G.; Jaque, D. *Nanoscale* **2013**, *5*, 7882.
(43) Tsai, M.-F.; Chang, S.-H. G.; Cheng, F.-Y.; Shanmugam, V.; Cheng, Y.-S.; Su, C.-H.; Yeh, C.-S. *ACS Nano* **2013**, *7*, 5330.
(44) Liu, S.; Chen, G.; Prasad, P. N.; Swihart, M. T. *Chem. Mater.* **2011**, *23*, 4098.
(45) Ye, X.; Zheng, C.; Chen, J.; Gao, Y.; Murray, C. B. *Nano Lett.* **2013**, *13*, 765.
(46) Norman, T. J.; Grant, C. D.; Magana, D.; Zhang, J. Z.; Liu, J.; Cao, D.; Bridges, F.; Van Buuren, A. *J. Phys. Chem. B* **2002**, *106*, 7005.
(47) Yu, H.; Chen, M.; Rice, P. M.; Wang, S. X.; White, R. L.; Sun, S. *Nano Lett.* **2005**, *5*, 379.
(48) Liu, X.; Wang, X.; Zhou, B.; Law, W.-C.; Cartwright, A. N.; Swihart, M. T. *Adv. Funct. Mater.* **2013**, *23*, 1256.
(49) Wei, T.; Liu, Y.; Dong, W.; Zhang, Y.; Huang, C.; Sun, Y.; Chen, X.; Dai, N. *ACS Appl. Mater. Interfaces* **2013**, *5*, 10473.
(50) Yu, W. W.; Chang, E.; Falkner, J. C.; Zhang, J.; Al-Somali, A. M.; Sayes, C. M.; Johns, J.; Drezek, R.; Colvin, V. L. *J. Am. Chem. Soc.* **2007**, *129*, 2871.
(51) Roper, D. K.; Ahn, W.; Hoepfner, M. *J. Phys. Chem. C* **2007**, *111*, 3636.
(52) Jiang, K.; Smith, D. A.; Pinchuk, A. *J. Phys. Chem. C* **2013**, *117*, 27073.
(53) Liu, X.; Atwater, M.; Wang, J.; Huo, Q. *Colloids Surf., B* **2007**, *58*, 3.
(54) Guo, L. R.; Panderi, I.; Yan, D. D.; Szulak, K.; Li, Y. J.; Chen, Y. T.; Ma, H.; Niesen, D. B.; Seeram, N.; Ahmed, A.; Yan, B. F.; Pantazatos, D.; Lu, W. *ACS Nano* **2013**, *7*, 8780.
(55) Xu, C.; Tung, G. A.; Sun, S. *Chem. Mater.* **2008**, *20*, 4167.
(56) Xi, D.; Dong, S.; Meng, X.; Lu, Q.; Meng, L.; Ye, J. *RSC Adv.* **2012**, *2*, 12515.
(57) Rand, B. P.; Peumans, P.; Forrest, S. R. *J. Appl. Phys.* **2004**, *96*, 7519.
(58) Xing, G.; Jiang, J.; Ying, J. Y.; Ji, W. *Opt. Express* **2010**, *18*, 6183.
(59) Yang, W. H.; Schatz, G. C.; Van Duyne, R. P. *J. Chem. Phys.* **1995**, *103*, 869.
(60) Moreno, F.; Albella, P.; Nieto-Vesperinas, M. *Langmuir* **2013**, *29*, 6715.

(61) Hsu, S.-W.; On, K.; Tao, A. R. *J. Am. Chem. Soc.* **2011**, *133*, 19072.
(62) Xie, Y.; Carbone, L.; Nobile, C.; Grillo, V.; D'Agostino, S.; Della Sala, F.; Giannini, C.; Altamura, D.; Oelsner, C.; Kryschi, C.; Cozzoli, P. D. *ACS Nano* **2013**, *7*, 7352.
(63) Ferry, V. E.; Sweatlock, L. A.; Pacifici, D.; Atwater, H. A. *Nano Lett.* **2008**, *8*, 4391.
(64) Aydin, K.; Ferry, V. E.; Briggs, R. M.; Atwater, H. A. *Nat. Commun.* **2011**, *2*, 517.
(65) Liu, X.; Lee, C.; Law, W.-C.; Zhu, D.; Liu, M.; Jeon, M.; Kim, J.; Prasad, P. N.; Kim, C.; Swihart, M. T. *Nano Lett.* **2013**, *13*, 4333.
(66) Kim, Y.; Park, K. Y.; Jang, D. M.; Song, Y. M.; Kim, H. S.; Cho, Y. J.; Myung, Y.; Park, J. *J. Phys. Chem. C* **2010**, *114*, 22141.